Chen, Yanjuan; Al-Neshawy, Fahim; Punkki, Jouni

Investigation on the effect of entrained air on pore structure in hardened concrete using MIP

Published in:
Construction and Building Materials

DOI:
10.1016/j.conbuildmat.2021.123441

Published: 19/07/2021

Investigation on the effect of entrained air on pore structure in hardened concrete using MIP

Yanjuan Chen[a*], Fahim Al-Neshawy[a], Jouni Punkki[a]

[a]Department of Civil Engineering, Aalto University, Espoo 02150, Finland

Abstract

The influences of entrained air on the pore size distribution and pore parameters of hardened mortar and concrete were investigated by MIP. It was found that the dosage of AEA does not affect the critical diameter for mortar or concrete. For air-entrained mortar with w/c of 0.38, the absence of superplasticizer leads to the critical diameter and threshold diameter shifting significantly to larger pores; and the AEA combined with SP can enhance the ink-bottle effect. As for air-entrained concrete, it is evident that the ITZ peak goes higher and shifts to coarser pores as the entrained air content increases; the ITZ fraction is most highly correlated with the air content (with R-square of 0.9385); also, it was indicated that more entrained air voids in concrete led to a high ITZ fraction. Therefore, together with larger ITZ pores (d_{c-ITZ}), it promotes the ITZ percolation.

Abbreviations: MIP, Mercury Intrusion Porosimetry; AEA, Air-entraining agent; SP, Superplasticizer; ITZ, Interfacial Transition Zone; ITZ peak, the second peak on the differential intrusion curve obtained from MIP; ITZ porosity, the porosity of the ITZ peak covered on the differential intrusion curve obtained from MIP; ITZ fraction, the fraction of ITZ porosity of total porosity; d_{c-ITZ}, critical parameters related to ITZ peak

Keywords: Entrained air; concrete; MIP; interfacial transition zone; porosity

1. Introduction

An important advance in concrete technology was the development of air-entrained concrete in the mid-1930s [1]. The entrained air voids in hardened concrete provide protection against frost damage. Especially in northern latitudes, air entraining is mostly required to secure the frost resistance of concrete. Air entraining increases the porosity of concrete and the correct volume and size of air voids are needed [2,3], which will affect the microstructure and pore structure of the hardened concrete. As we know, porosity is decisive in concrete technology; it affects both the mechanical and durability properties of concrete. Typically, concrete technology is about reducing the porosity to make the concrete both stronger and more environment-resistant, whereas the air-entraining agent (AEA) deliberately creates pores in the concrete to prevent the concrete from suffering from freezing. Both attract our interest to explore how the entrained air affects the whole pore system in air-entrained concrete.

Further, AEA was used to introduce air voids intentionally during the production of concrete. Entrained air voids provide a relief system for internal ice pressure by providing internal voids to accommodate the volume expansion caused by freezing water. Entrained air voids are discrete, individual bubbles of spherical shape, usually in an amount of about 2–6% by volume of the concrete. They are generally assumed to be distributed uniformly throughout the cement paste, are not connected with each other and cannot form a continuous flow channel, and have no effect on the permeability of concrete [4]. However, it is not the case as expected that the air voids have no effect

*Corresponding author.
E-mail: yanjuan.chen@aalto.fi, yanjuan1105@gmail.com.

on the permeability of concrete. Entrained air voids disturb the distribution of pores and the particle size, which may cause a significant change in the microstructure of the hardened concrete, and particularly in its pore structure. This change may, in turn, influence the permeability and strength of the hardened concrete. Besides, the entraining of air voids is accompanied by variation in the cement, water, and concrete content. For instance, increasing air content may be accompanied by a decrease in the aggregate content if the cement content and effective water–cement ratio (w/c) are kept constant; therefore, the actual contribution of the entrained air voids cannot be isolated.

In general, the studies about the effect of entrained air on hardened concrete mainly deal with three aspects: 1) the influence on mechanical properties such as strength. For instance, a well-known study revealed that every 1% increase in air content decreases the compressive strength of concrete by 4–6% [5]; 2) the influence on frost resistance; 3) the effect on transport properties and microstructure. With respect to 2), extensive previous studies focused on characterizing the void system and determining its frost resistance [2,6,7]. The spacing factor, specific surface, and total content of air voids were usually employed to characterize the void system. Aspect 3) is the foundation, which is closely related to the pore structure and can offer theoretical support to aspects 1) and 2). Concerning the studies of transport properties, there was an earlier dispute over the air voids increasing or decreasing the transport coefficient (such as the conductivity coefficient) [8,9]. H.S Wong et al. in 2011 carried out a systematic investigation into the influence of entrained air voids on the microstructure and bulk transport properties of concrete under different exposure conditions (saturated and non-saturated) [10]. They concluded that entrained air voids can increase or decrease the transport properties, depending on the transport mechanism under consideration, and the moisture content of the voids. Under non-saturated conditions, empty air voids act as insulators and the bulk electrical conductivity is decreased. However, saturated air voids behave as conductors and increase the electrical conductivity. Thus, every 1% increase in air content increases the transport coefficient by about 10% or decreases it by 4%, depending on whether the air voids act as conductors or insulators. Besides, air entrainment increases the gaseous diffusivity and permeability by a factor of up to 2–3 with the highest air contents, regardless of the w/c ratio, curing age and conditioning regime. Later, P. Heede et al. in 2013 reported that AEA increased the water sorption under vacuum and the apparent gas permeability [11]. This seems consistent with H.S Wong's conclusion. However, water capillary absorption in air-entrained concrete has also been studied by Li et al. (2016) [12]and Zhang et al. (2017) [13]. Both results showed that the penetration depth and absorbed water are significantly reduced by air entrainment due to the larger artificial pores interrupting the fine pores of the hardened cement paste and resulting in incomplete filling with water. Here it seems the air voids were unsaturated and behaved as insulators. Zhang et al. in 2018 [14] compared the chloride diffusion coefficients of air-entrained concretes (and ordinary concrete as reference) using the RCM method The results showed that the diffusion coefficients for concretes with 0.53 water–binder ratio (w/b) did not decrease as the air content increased, even though all the concretes had the same exposure condition (with similar saturation). The same scenario for a lower water–binder ratio (0.35) group of concretes showed that the highly air-entrained concrete had a higher value of chloride diffusion, and the reference concrete and moderately air-entrained concrete had similar values. This phenomenon apparently cannot be explained only by the insulator and conductor theory.

When it comes to the transport properties (such as oxygen permeation, chloride transport, water absorption, etc.) of concrete, the transport media, transport substances, and initial conditions are definitely involved together. Transport is dependent on 1) the intrinsic pore structure, involving the pore size distribution, connectivity, tortuosity, ITZ (interfacial transition zone), particles distribution, etc. that characterize the transport medium; 2) the properties of the transport substances (water, chloride, carbonate, sulfate, etc.), where generally water serves as a carrier for the ions of the substances; 3) the initial conditions (prior exposure history).

Concerning the transport properties of air-entrained concrete, the insulator and conductor theory for air voids is reasonable from the aspect of prior exposure history and there is a need to seek an explanation from the aspect of the intrinsic pore structure. Ultimately, entrained air voids affect the pore size distribution, particle distribution and even the ITZ of the pore structure of concrete. More studies worked on the influence of air voids on the microstructure of concrete, especially the influence on the interfacial transition zone (ITZ). H. S. Wong studied the air void–paste interface with BSE and pointed out that the porosity near the air void interface is about 2–3 times that of the bulk paste, and the width of the interface is around 30 μm from the void boundary [10]. The width of the void–paste interface is in the range typically reported for the aggregate–cement ITZ width of 20–50 μm [15]. The result also showed that for a given ITZ width of 30 μm (the thickness of the layer of paste around an air void or an aggregated particle that is more porous than bulk paste), increasing the air content from 0.5% to 8.2% increases the ITZ fraction from 0.4–0.9. Gao et al. analyzed the effect of air voids on the paste–aggregate ITZ by microhardness under the condition of similar total porosity; the results showed that the width of the ITZ decreased and the microhardness of the ITZ increased with the decrement of the average air void size, which will result in a decrease in the loss of compressive strength [16]. Besides, Amin Ziaei-Nia et al. simulated thermal stress in concrete with finite element software and suggested that air bubbles can reduce the plastic strains in the ITZ [17]. However, all the above literature did not consider ITZ percolation for the whole continuous pore system. As the entrained air affects the ITZ, it will affect ITZ percolation.

With respect to the influence of entrained air on the microstructure of concrete, less attention has been dedicated to the effect of entrained air on the continuity of the pore system of concrete, which is necessary for better understanding and improvement. Understanding how entrained air voids can affect the continuity of the pore system is vital for estimating the transport properties of air-entrained concrete. This study aims to investigate the effect of entrained air on the pore size distribution of concrete and some critical pore parameters. MIP measurement was adopted to obtain the pore information because it can evaluate a much wider range of pore sizes than any alternative method practiced currently. Besides, some pore structure parameters deduced from MIP measurement can be used in analytical and empirical property–microstructure models.

2. Review of the methodology of Mercury Intrusion Porosimetry (MIP)

Mercury intrusion porosimetry (MIP) has become one of the most widely used methods for obtaining pore information of cementitious materials since it was introduced for concrete by L. Edel'man et al. in 1961 [18]. The technique is relatively easy and quick to perform, takes less than an hour to complete, and has a great capacity to evaluate a much wider range of pore sizes than any alternative method practiced currently. Despite these merits, there is still much debate about the reliability of this method, due to several inappropriate assumptions and drawbacks. Firstly, the pore size distribution obtained by MIP is based on the Washburn equation model. In this model, it is assumed that the pores are taken as cylinders of a diameter that departs from the reality of the pore system, which has pores of different sizes and shapes. Another assumption is the contact angle. It is affected by several parameters such as properties of the cement paste, the characteristics of the pores, and mercury itself. The difference in contact angle values depends on the technique used to measure them and it is difficult to decide which one gives the correct value. A solution to determine the uncertainty of the contact angle is to select a conventional value for it, which would lead to a constant error in the results. Whatever value is used in the test, it should be reported with the results.

Another uncertainty of MIP results is the presence of ink-bottle pores, which leads to hysteresis and mercury retention in the pores. Yet another inaccuracy of the MIP test is the alteration of the initial pore structure. One factor is the drying pretreatment of the MIP specimen, which may change the initial pore structure. Another is that the pressure involved in intrusion produces alteration of the pore structure, especially at high pressure. It was suggested that high pressure applied on the mercury for intrusion may result in temporary and permanent alteration in the microstructure of the cement paste [19,20]. However, it was reported that the error due to alteration of the pore structure is no more than 3% [21]. It was generally expected that the specimen under test would be damaged only if the porosity was very high, or if there was a significant number of closed pores [22]. Thus, the effects of these factors can be neglected without introducing significant error. In addition, the literature reports that the specimen size influences the MIP results [23]. The sample size stands for a characteristic length scale rather than the sample volume. The pore size distribution and connectivity of pores have significant effects on the length scale. If the length scale is below the minimum sample size, there will be no size effect on the MIP results [24]. Typical acceptable specimen volumes used in commercially available instruments for MIP tests range from a few cm^3 up to 15 cm^3 [25].

However, MIP still has excellent value in cement and concrete research. First of all, MIP allows horizontal comparison of relative changes in different pore systems and provides a comparative assessment of the refinements that are taking place within a given system [26]. Furthermore, several meaningful parameters deduced from MIP tests can be employed in establishing property–microstructure relations [27,28]; for instance, the critical diameter from MIP results can be used in the Katz–Thompson equation to predict the permeability of cement paste. Hence, all the influencing factors (such as the sample preparation, sample drying method, contact angle, surface tension, etc.) should be fixed in the same conditions when making the pore structure comparison based on MIP results.

MIP measures the continuous pore system, and closed pores below the threshold accessible to mercury are excluded. However, large pores due to entrained air or compaction voids in air-entrained concrete are mostly interconnected and therefore can be reached via smaller capillary pores. This should affect the pore system detected by MIP. Thus, this is of interest in this research.

3. Experiment

3.1 Materials and preparation of air-entrained concrete specimens

Portland limestone cement CEM IIA 42.5 R was adopted as the cementitious material for the air-entrained concrete. The aggregate was granitic gravel with a 16 mm nominal maximum size. Air-entraining agent (AEA) ILMA-PARMIX was used in the concrete for creating stable air bubbles. The mix designs of test concrete were aimed to explore the effect of air-entraining agent on the pore structure of concrete, so no superplasticizer (SP) was added. The water–cement ratio for every concrete was higher than 0.6 to ensure suitable workability. The different concrete mix designs investigated are described in Table 1. The air content of the hardened concrete was determined with the pressure-saturation method according to the old Finnish standard SFS-4475.

Table 1. Mix composition of air-entrained concretes.

Mix	Cement (kg/m^3)	Water–cement ratio	Aggregates (kg/m^3)	AEA (% of cement)	Aggregate volume fraction	Air content (%)
A3-0.01	262	0.65	1964	0.01	0.73	3.0
A5-0.02	262	0.65	1910	0.02	0.71	5.0
A6-0.03	262	0.65	1883	0.04	0.70	6.5
B2-0	285	0.63	1890	0.00	0.70	1.6
B3-0.01	285	0.63	1837	0.01	0.68	3.5

Cubic concrete beams (100 mm · 100 mm · 500 mm) for the mixes were cast in the laboratory. After demolding at an age of 24 hours, the concrete samples were exposed for 28 days in a curing chamber at 20 °C and 95% RH. Subsequently, 3 parallel cylindrical samples were drilled from the center part along the centerline of the square prism for every concrete. All the drilled cylindrical samples had the same diameter of 24 mm, and the variation of height was from 20 to 32 mm. For different concretes, samples were drilled around the same location. Before tests, the samples were vacuum-dried for 3 weeks.

3.2 Materials and preparation of air-entrained mortar specimens

Portland cement CEM/B-M (S-LL) 42.5 N containing blast furnace slag was selected as cementitious material. The sand adopted was granitic gravel with a maximum size of 2 mm. Air-entraining agent Master Air 100 and polycarboxylate ether-based (PCE) superplasticizers (named MasterGlenium SKY 600) were used in the mortar, which were both produced by BASF SE.

The air-entrained mortar with lower water–cement ratio was designed with the aim of investigating the effect of the dosage of AEA on the pore structure of the mortar. Due to the lower water–cement ratio, superplasticizer (SP) was added. Four groups of air-entrained mortar mix with 0.38 w/c and containing 0.45% sand by volume were prepared. The dosage of air-entraining agent varied from 0–0.07% of cement by weight, and the flow diameter was 160–200 mm (test according to ASTM C 1437) after 60 min with a superplasticizer dosage of 0.6% of cement. The air content in the hardened mortar was also determined with the pressure-saturation method, which is demonstrated in Table 3. The code of the air-entrained mortar was denoted as, e.g., M-0.6%-0.07%, the first number indicating the dosage of superplasticizer and the second number indicating the dosage of air-entraining agent. Also, one blank set of air-entrained mortar with the same mix design but without superplasticizer was prepared and denoted as M-0-0.07%.

The specimens (40 mm· 40 mm· 160 mm) for the mortar mixes were cast and cured for 28 days with the same procedure as the concrete. Cylindrical samples with diameter of 14 mm and height 15 mm for MIP tests were drilled from the center of the mortar specimens. Before tests, the cylindrical samples (diameter: 14 mm, height: 15 mm) were dried under the condition of 50 °C and relative humidity of 50–60 % for 48 hours.

3.3 MIP test

The choice of contact angle does not affect the results obtained for total porosity. Still, it has an impact on the pore size distribution, and the threshold diameter determined [29]. The contact angle should be determined concerning the cement paste's age, composition, pretreatment method, etc. The most common quoted values for the contact angle are 130° and 140°. Considering the sample's maturity and pretreatment method in this study, the assumed contact angle was 130° for the mortar and 141.3° for the concrete, respectively. The surface tension was kept at 0.480 N/m, and the equilibration time was chosen to be 50 s for each pressurization or depressurization step during testing.

MIP measurements were performed with a Micromeritics Autopore IV 9500 version 2.00, which is capable of measuring pore diameters from 0.003 to 1000 μm. The maximum intrusion can reach 413.7 MPa, corresponding to 0.002 to 0.003 μm. In this measurement, it was found that there was no mercury in the samples at a level up to 206.8 MPa (corresponding to the measurable diameter of around 0.007 μm). The dilatometers for the actual MIP instrument are of 5 cc for the mortar samples and 15 cc for the concrete samples, respectively. All the MIP results presented in this paper are obtained from the average of at least three individual measurements.

Three replicates of ordinary Portland cement (OPC) mortar samples with w/c of 0.38 were employed to check the reproducibility of the MIP measurements. A variety of tested parameters are listed in Table 2. For an overview of the data, the sample weight is around 5 g. The difference in total porosity between the maximum and the minimum value is $0.189\ \%$ with a coefficient of variation (CV) of $1.09\ \%$. The CV for other parameters, i.e., bulk density and skeletal density, are all less than 1%. This indicates that the MIP test exhibited a good reproducibility in this study.

Table 2. Data of three replicates for OPC mortar (w/c=0.38, 28 days, with 0.6% SP).

Sample no.	Weight (g)	Total porosity (%)	Bulk density (g/mL)	Skeletal density (g/mL)
1	4.7530	9.168	2.1974	2.4193
2	5.0590	9.357	2.1905	2.4167
3	4.8500	9.201	2.1957	2.4182
Average	4.8873	9.242	2.1945	2.4181
STDEV	0.1564	0.1009	0.0036	0.0013
CV (%)	3.19	1.09	0.16	0.054

3.4 Scanning electron microscopy (SEM) test

In MIP studies, changes in the pore structure of air-entrained mortar were observed for different entrainments. The microscopic studies aimed to clarify these changes in pore structures and morphology due to chemical admixtures.

The microscope used was a Zeiss GeminiSEM 300. Before the SEM test, the mortar sample preparation method was the same as for the MIP tests. After the samples were dried at 50 °C for 48 hours, their surface was gold-treated to make them conductive for SEM studies.

4. Results and discussion

4.1 Review of pore information acquisition from MIP

MIP data is obtained by recording the volume of mercury that intrudes in the porous specimen as a function of pressure. A pressurized curve is the curve of the intruded volume of mercury (V) vs. applied pressure (P); however, this curve cannot be used to obtain information about the pore structure parameters. The readings of the intruded volume need to be corrected and normalized in a variety of ways, such as dividing the intruded volume by the specimen mass (resulting in units of cm^3/g or mL/g) or by the specimen bulk volume. In typical plots, the ordinate includes the cumulative intruded volume per unit specimen mass or per unit bulk specimen volume, and the percent of the total intruded volume; the x-axis expresses the pressure or pore size (pore radius or diameter). Values of the pore radius corresponding to the specific value of pressure at any time during the experiment can be calculated through the equilibrium equation [4]:

$$r_P = \frac{-2\gamma_m \cos\theta}{P} \tag{1}$$

where r_p is the pore radius (m), γ_m is the surface tension between the mercury and the pore wall (N/m), θ is the contact angle between the mercury and the pore wall (degree), and p is the pressure applied on the mercury to intrude the pore (N/m^2). Some advanced equipment directly offers the value of the pore radius or diameter from the experimental data.

The most common parameters used to characterize cement-based materials' pore structure include the porosity, hydraulic radius, specific surface area, threshold diameter, and pore size distribution, all of which can be provided by the MIP method. However, it should be kept in mind that the MIP method cannot provide the absolute value of parameters, and neither can other experimental methods. Each method only gives a characteristic value that depends on the principle of the technique used and the nature of the specimen tested. Therefore, we should not expect a perfect agreement between the values of the parameters determined by MIP and by other methods. For instance, the total porosity determined by MIP is a kind of effective porosity, not the absolute porosity, and indicates the total volume of mercury intruded (intrudable porosity).

The most commonly used plots from MIP are summarized as the following: cumulative intrusion volume vs. pressure or diameter (cumulative pore volume curve); cumulative porosity vs. diameter (cumulative porosity curve); differential intrusion volume vs. diameter; differential surface area vs. pressure (or vs. diameter); differential surface area vs. pressure (or vs. diameter).

4.1.1 Pore parameters determined from MIP

The most frequently used parameters in analytical and empirical property-microstructure models are the intrudable porosity (ϕ_{in}), the critical pore diameter (d_c) and the threshold pore diameter (d_{th}), which can be determined from the cumulative pore volume curve and differential pore volume curve. ***The intrudable porosity*** can be obtained from the value of the highest point on the cumulative pore volume curve. For the cumulative pore volume curve, when the y-axis expresses the intruded volume per unit specimen mass, the calculation of the intrudable porosity requires the specimen's bulk density. The value of the bulk density can be deduced from the amount of mercury displaced by the sample in the specimen cell after the initial filling at low pressure, which is a known volume. The calculation of the intrudable porosity from the value of the cumulative pore volume can be expressed as below:

$$\phi_{in} = \frac{v_t \cdot m_{sample}}{m_{sample}/\rho_{bulk}} = v_t \cdot \rho_{bulk} \tag{2}$$

and if the skeletal density is also a known value like the bulk density, the intrudable porosity can also be calculated with Equation (3):

$$\phi_{in} = \frac{m_{sample}/\rho_{bulk} - m_{sample}/\rho_{skeletal}}{m_{sample}/\rho_{bulk}} = 1 - \frac{\rho_{bulk}}{\rho_{skeletal}} \tag{3}$$

where ϕ_{in} is the intrudable porosity, $v_t\,(mL/g)$ is the total intrusion volume at the highest pressure, $m_{sample}\,(g)$ is the mass of the sample, $\rho_{bulk}\,(g/mL)$ is the bulk density at the lowest pressure, and $\rho_{skeletal}\,(g/mL)$ is the skeletal density at the highest pressure. In this paper, we take the intrudable porosity as the total porosity according to convention.

The critical diameter corresponds to the steepest slope of the cumulative pore volume curve and the highest point on the corresponding logarithmic differential pore volume curve, as shown in Figure 1. The critical diameter is the most frequently occurring pore size in the interconnected pores that allows the maximum percolation throughout the pore system, which controls the transmissivity of materials and is more often used to examine the effects of factors such as the water–cement ratio, temperature, etc., on the pore structure's change.

The threshold diameter was introduced to consider the possibility that large pores can be present in the interior of the cement paste but have access to the exterior only through small size channels of the continuous pore system. Winslow and Diamond in 1970 defined the threshold diameter as the minimum diameter of channels that are essentially continuous through the cement paste [30]. It should be emphasized that the critical diameter describes the size of the pores, while the threshold diameter describes the size of the transport paths (channels), both of which are not even of the same order. The threshold diameter occurs at a larger radius [31]. Young in 1974 suggested that above the threshold diameter only the interconnected large capillary pores are intruded, and below the threshold diameter the void space between C-S-H gel “needles” is filled, which represents a large portion of the intrudable volume [32]. Diamond proposed that “choke points” correspond to the narrowest place of the constricted long percolating chains. The long percolating chains, made up of various sizes of pores, constitute the capillary pores in the cement paste [33]. He took the pore diameter at the choke points as the threshold diameter. Also, he suggested that when the mercury pressure is enough for mercury to flow through these constrictions, a large portion of the whole pore system is simultaneously intruded, which produces a very steep rise in the curve of cumulative pore volume vs. pore diameter. The first inflection point on the curve where the slope increases abruptly indicates the threshold diameter, which marks the onset of percolation. Above the threshold diameter there is comparatively little mercury intrusion, and immediately below it the great portion of intrusion commences. In a similar way, other researchers also associate the threshold diameter with the point where the initial rapid increase in the cumulative porosity curve occurs [34,35].

It has been found that the permeability of cement paste is more sensitive to the threshold diameter than to the total porosity, both of which parameters can be determined using the MIP technique [36,37]. The increased chloride permeability of pastes with a high water–cement ratio is most closely correlated with the increased threshold diameter; this is probably because the threshold pore size is the widest and most accessible path for fluid transport in the cement paste [38].

Researchers are still in dispute over the determination of the threshold pore diameter. The selection of the first inflection point on the cumulative intrusion curve tends to more subjective, thereby leading to error. Liu and Winslow made tangents to the curve from below and above the first inflection point and used the intersection point from the tangents to determine the threshold pore diameter [38]. This tangent method is more objective and reasonable compared to the first inflection method, as has been discussed by Hongyan Ma [39]. The definitions of the three parameters adopted in this research are presented in Figure 1. Our research focuses on the investigation of the three most used parameters derived from the cumulative pore volume curve and differential pore volume curve from MIP.

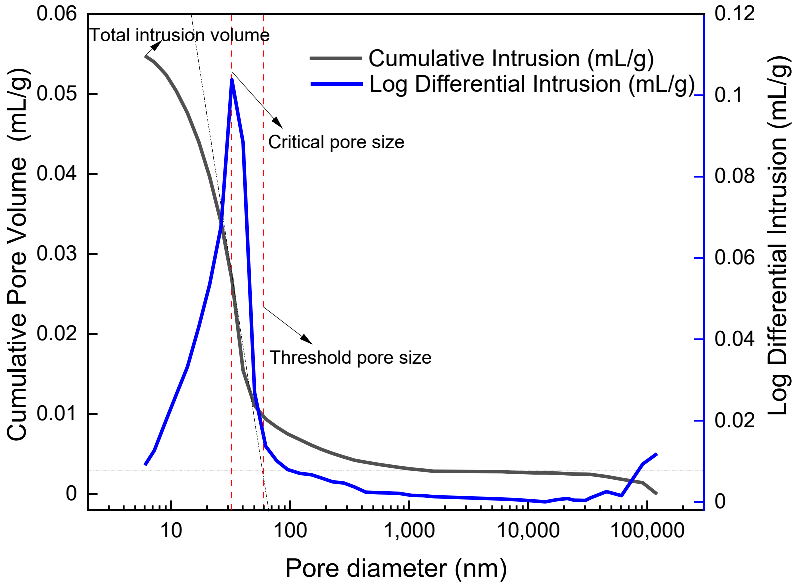

Figure 1. Definition of parameters from MIP tests.

4.1.2 Hysteresis and entrapment of mercury

Besides the three main parameters stated above, hysteresis between the intrusion and extrusion curves can be observed from the cumulative intrusion curve. This indicates that the extrusion path during depressurization does not follow the intrusion path during pressurization. In addition, the intrusion–extrusion cycle does not close when the initial pressure is reached, indicating that some mercury remains entrapped in the pore system after complete depressurization. Thus, the two phenomena, the entrapment of mercury in the pore system and hysteresis between the intrusion and extrusion curves, can be revealed by the cumulative intrusion curve, as shown in Figure 2.

Considering the hysteresis between the intrusion and extrusion curves, the pore size distribution plots derived from the volumes and pressures obtained from the intrusion curve will be different from the corresponding plots from the extrusion curve. Typically, researchers use the first cycle's intrusion curve to plot the pore size distribution. After reducing the pressure to atmospheric pressure, various amounts of mercury remain irreversibly entrapped in the specimen, depending on the porous material. The amount of entrapped mercury can vary from a negligible portion up to nearly the total volume of pores, depending on the pore structures of the materials. The literature states that $1/3$ to $1/2$ of the intruded mercury may not exit the spontaneous pores upon depressurization [40]. Feldman has reported that the residual mercury in higher in plain cement pastes, and lower in blended pastes, which depends on their composition [41].

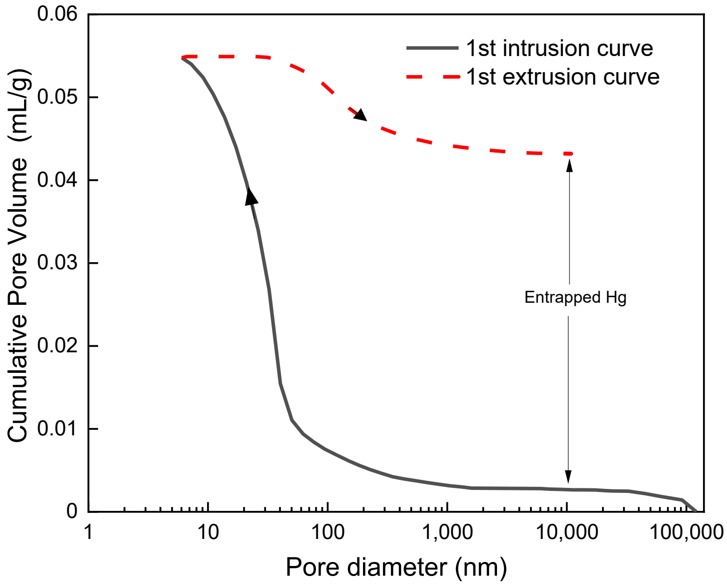

Figure 2. Intrusion–extrusion hysteresis curves and entrapment of mercury in mortar specimen. The arrows indicate the direction of intrusion and extrusion.

The non-closure hysteresis loop between the intrusion and extrusion curves is a universal feature of MIP and can be observed in nearly all specimens during MIP measurement. The most commonly used theories that explain the hysteresis are the ink-bottle effect and differences in the contact angle. Other theories are the pore potential (energy barrier theory), the surface roughness of the pore walls, contamination of the material's surface by mercury, and percolation/connectivity theory (network effect). Connectivity theory is similar to the ink-bottle effect, which involves pores connected by continuous paths/channels. However, none of the mechanisms can by themselves explain the phenomena of hysteresis and entrapment sufficiently. The phenomena are probably a consequence of more than one mechanism. Our intention is not to discuss the rationality of the various theories. However, the aim is to compare these two phenomena (hysteresis between the first cycle's intrusion and extrusion curves, entrapped mercury after the first depressurization) between plain mortar and air-entrained mortar. It is assumed that the "ink-bottle effect" can interpret the phenomena, despite having flaws in the explanation. In the porous system, the large pores (wide cavity/pore) are connected by smaller constrictions (neck/narrow throat). Mercury enters the pore cavity at a pressure that is determined by the neck entrance instead of the actual pore cavity size. However, the wide body of the ink-bottle pore cannot empty through the throat pore at low pressure (e.g., atmospheric pressure) during depressurization, leaving the mercury retained in the wide inner pore. Also, the trapped mercury can be explained by the breaking of the mercury column in the narrow neck of an ink-bottle pore during its rapid emptying such that the mercury is trapped in the wide ink-bottle cavity. The amount of entrapped mercury can serve to measure the pore volume of the ink-bottle pores. The retention factor was introduced to quantify the entrapped mercury [42], which is determined by Equation (4).

$$R = \frac{V_{ret}}{V_{max}} \tag{4}$$

where R is the retention factor (unitless), V_{ret} is the retained volume of mercury after the first cycle of intrusion–extrusion is completed (mm^3), and V_{max} is the total volume of intruded mercury at the maximum pressure (mm^3). We adopt the amount of entrapped mercury to examine the ink-bottle effect in different pore systems.

4.2 Analysis of air-entrained mortars

4.2.1 Results from MIP

The values of the pore parameters and entrapped mercury (calculated from Equation (4)) for every sample are summarized in Table 3.

Table 3. Values of entrapped mercury for air-entrained mortars ($w/c = 0.38$, 28 days).

Sample no.	Total porosity (%)	Critical diameter (nm)	Threshold Diameter (nm)	Retention factor (%)	Air content in hardened mortar (%)
M-0.6%-0%	9.36	32.38	50.31	73.95	2.26
M-0.6%-0.04%	12.14	32.39	59.56	73.69	3.69
M-0.6%-0.07%	12.55	32.32	60.56	81.54	6.94
M-0-0.07%	11.09	40.94	80.98	74.69	4.40

Figure 3 shows the differential and cumulative plots for all the mortars. All the plots were based on the average from three measurements, with an accuracy of $\pm 5\%$. As depicted in Figure 3 (a), (b), and (c), the general rule is as expected that the total porosity increased with increase of the dosage of the AEA when the SP was kept constant. However, the values of the critical diameter are nearly consistent (32.38, 32.39, and 32.32 as shown in Table 3). The values of the threshold diameter increased for concretes with AEA, as compared to concretes without AEA (comparing 59.56 and 60.56 to 50.31 as shown in Table 3), but without a significant difference as the amount of AEA increased (59.56 and 60.56, respectively). Besides, it was found that the trend of variation for the total porosity was consistent with the change of air content in the hardened mortar.

Besides, it was observed that the critical diameter and threshold diameter for sample M-0-0.07% shifted to larger pores compared to others. This reveals that the presence of SP results in the decrease of the critical diameter and threshold diameter of air-entrained mortars. It can be speculated that the superplasticizer affects the hydration that the pore system of mortars varied, since Winslow and Diamond in 1970 [30] found that the threshold decreased with the hydration for cement paste. Also, Diamond in 2000 reported that the threshold radius will decrease with the curing time, and as the water–cement ratio decreases [33]. It can be deduced that the curing time and water–cement ratio affected the threshold radius, which is principally attributed to the hydration of cement.

In the next section, the SEM observation for all mortar samples will render more detailed information about the microstructure.

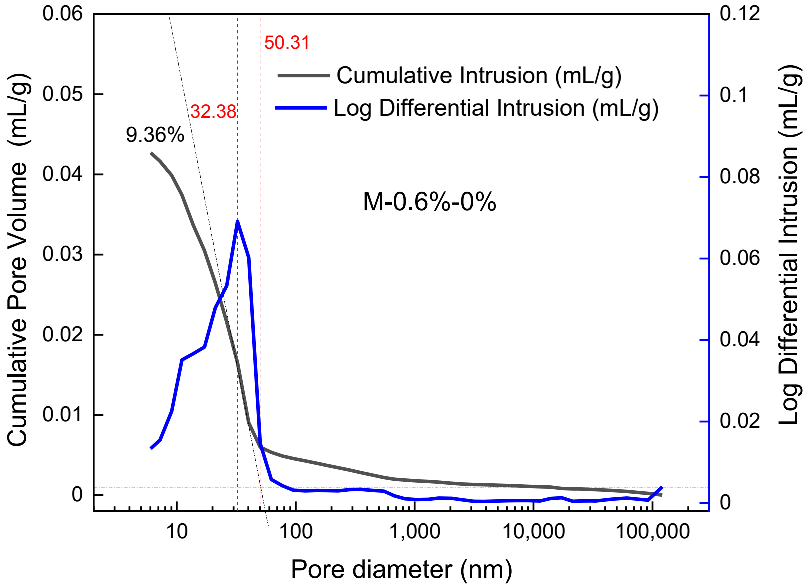
0.06
0.05
0.04
0.03
0.02
0.01
0
0.12
0.1
0.08
0.06
0.04
0.02
0
50.31
32.38
9.36%
Cumulative Intrusion (mL/g)
Log Differential Intrusion (mL/g)
M-0.6%-0%
Cumulative Pore Volume (mL/g)
Log Differential Intrusion (mL/g)
10
100
1,000
10,000
100,000
Pore diameter (nm)

(a)

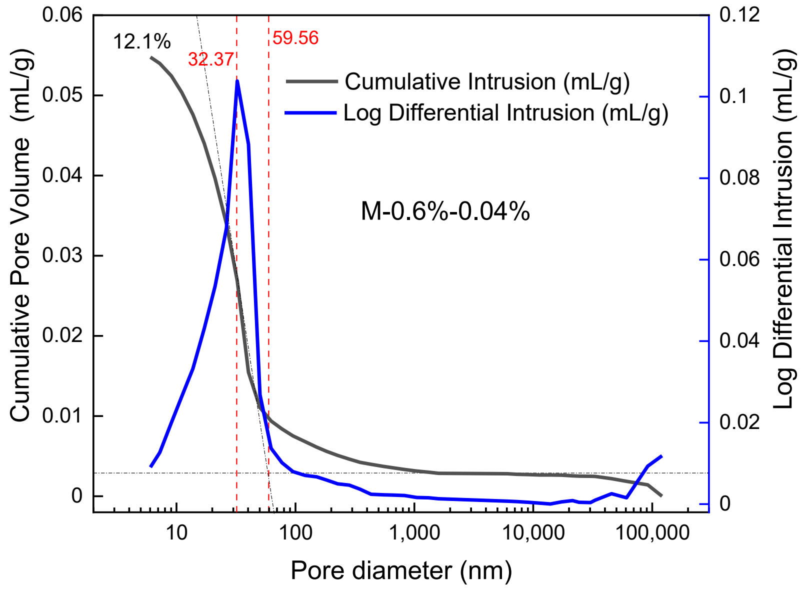
0.06
0.05
0.04
0.03
0.02
0.01
0
0.12
0.1
0.08
0.06
0.04
0.02
0
12.1%
32.37
59.56
Cumulative Intrusion (mL/g)
Log Differential Intrusion (mL/g)
M-0.6%-0.04%
Cumulative Pore Volume (mL/g)
Log Differential Intrusion (mL/g)
10
100
1,000
10,000
100,000
Pore diameter (nm)

(b)

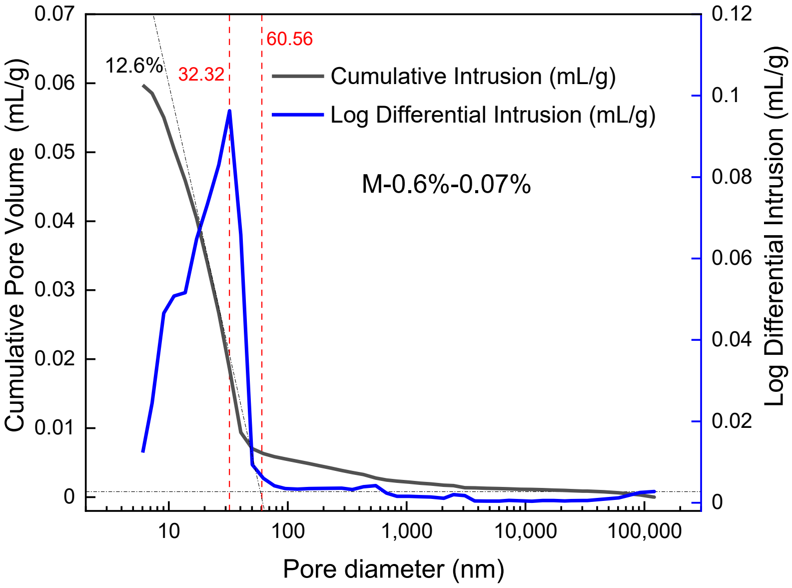

(c)

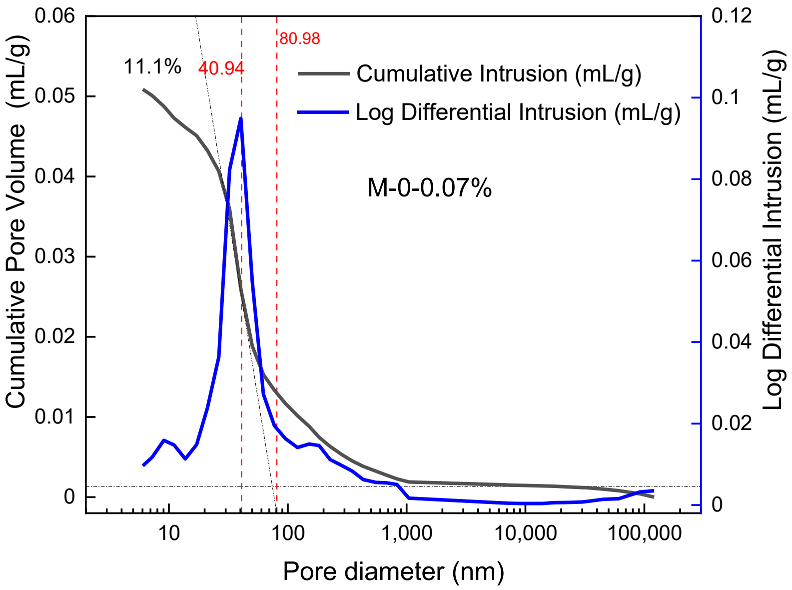

(d)

Figure 3. Cumulative and differential plots for air-entrained mortars.

Figure 4 presents the hysteresis curves and amounts of entrapped mercury after the first pressurization–depressurization cycle. It was observed that the values of entrapped mercury for all mortars vary from 73.7% to 81.5%, as shown in Table 3, a significant portion of the total intruded mercury. Ritter reported that the entrapped mercury in porous materials could reach 80–85% of the total volume of the pores [43]. For all the samples, the samples with the highest content of SP and AEA have the most significant retention factor (reaching 81.54%). This indicates that the addition of

SP and AEA can enhance the ink-bottle effect, since the tortuosity of the pores' path increased in the pore system, probably owing to the fact that the addition agents affect the hydration of the mortar.

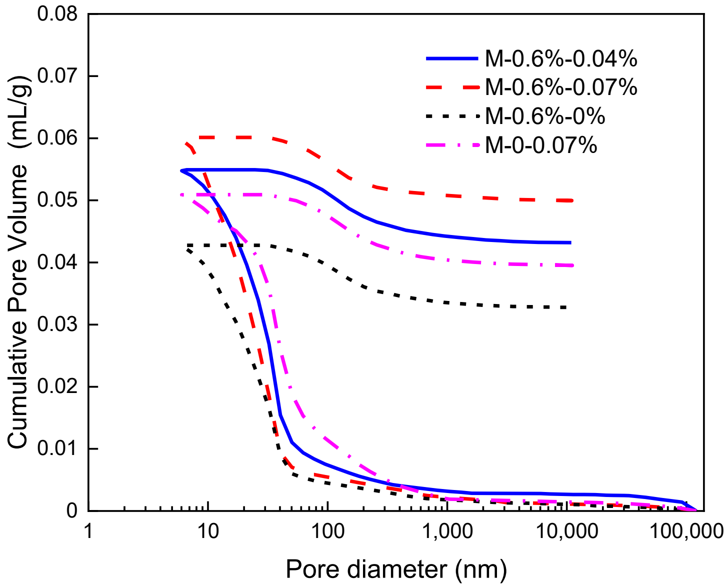

Figure 4. Intrusion–extrusion hysteresis curves and entrapment of mercury for air-entrained mortars.

4.2.2 Results from morphology analysis

MIP measurement in combination with micrographs seems to be a promising technique to determine the pore structure by the microscopy technique.

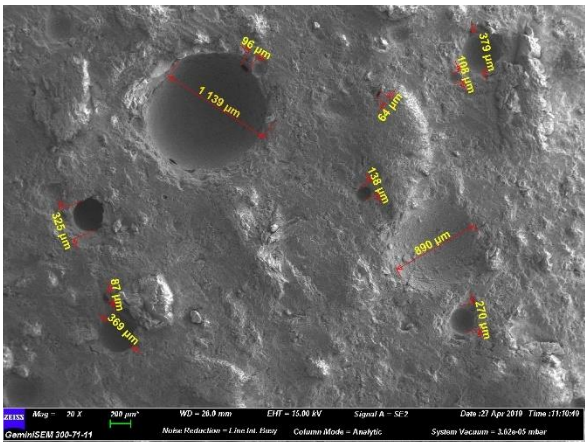

M-0.6%-0%

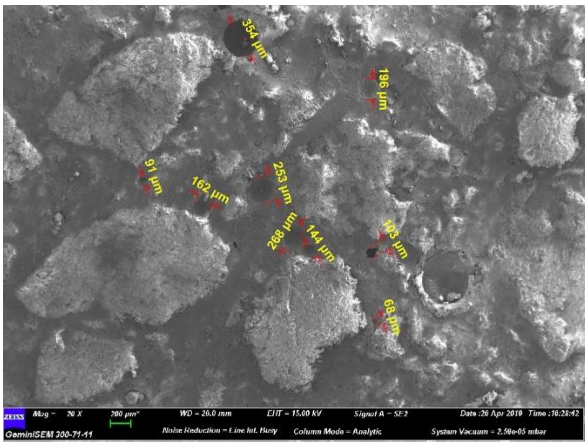

M-0.6%-0.04%

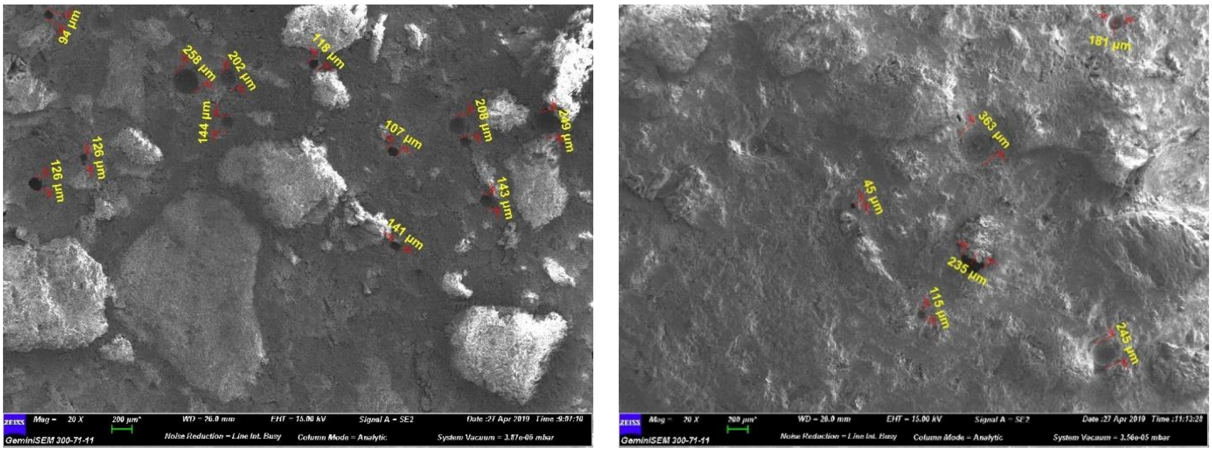

M-0.6%-0.07% M-0-0.07%

Figure 5. SEM images presenting the air voids in air-entrained mortars.

ASTM terminology relating to concrete defines as entrapped air voids having a size above 1 mm and as entrained air voids with a diameter between 10 μm and 1 mm according to ASTM C 125. The entrained air voids mainly protect concrete against freezing and thawing; but large entrapped air voids are not altogether beneficial to frost resistance. The Figure 5 SEM images present the air voids observed in same size of zone for air-entrained mortars. The air voids are observed to be nearly spherical and isolated from other air voids. Air voids are discrete and uniformly distributed throughout the cement paste and are not interconnected with each other. The more detailed information about the air pores is summarized in Table 4. It can be seen that the sample M-0.6%-0.07% is the ideal air-entrained mortar with the most uniform distribution and reasonable size of air voids, while the sample M-0-0.07% has a smaller amount of air voids compared to other samples due to the absence of SP. The observation results verified the testing result that sample M-0.6%-0.07% has the optimal air content in hardened air-entrained mortar.

Table 4. Description of air voids observed with SEM.

Sample no.	Range of diameter (μm)	Distribution description	Number of air voids observed
M-0.6%-0%	64–1139	Voids have the most uneven size, from 64 μm to 1139 μm. And voids with diameter above 200 μm are most common.	11
M-0.6%-0.04%	45–356	Voids have an even size, compared to above. And voids with diameter less than 200 μm are most common.	11
M-0.6%-0.07%	94–258	Voids have the most uniform size, compared to other samples. And voids with diameter around 120 μm occupy the main portion.	12
M-0-0.07%	46–365	Fewer voids were observed, compared to other samples, and voids are not easily detected.	8

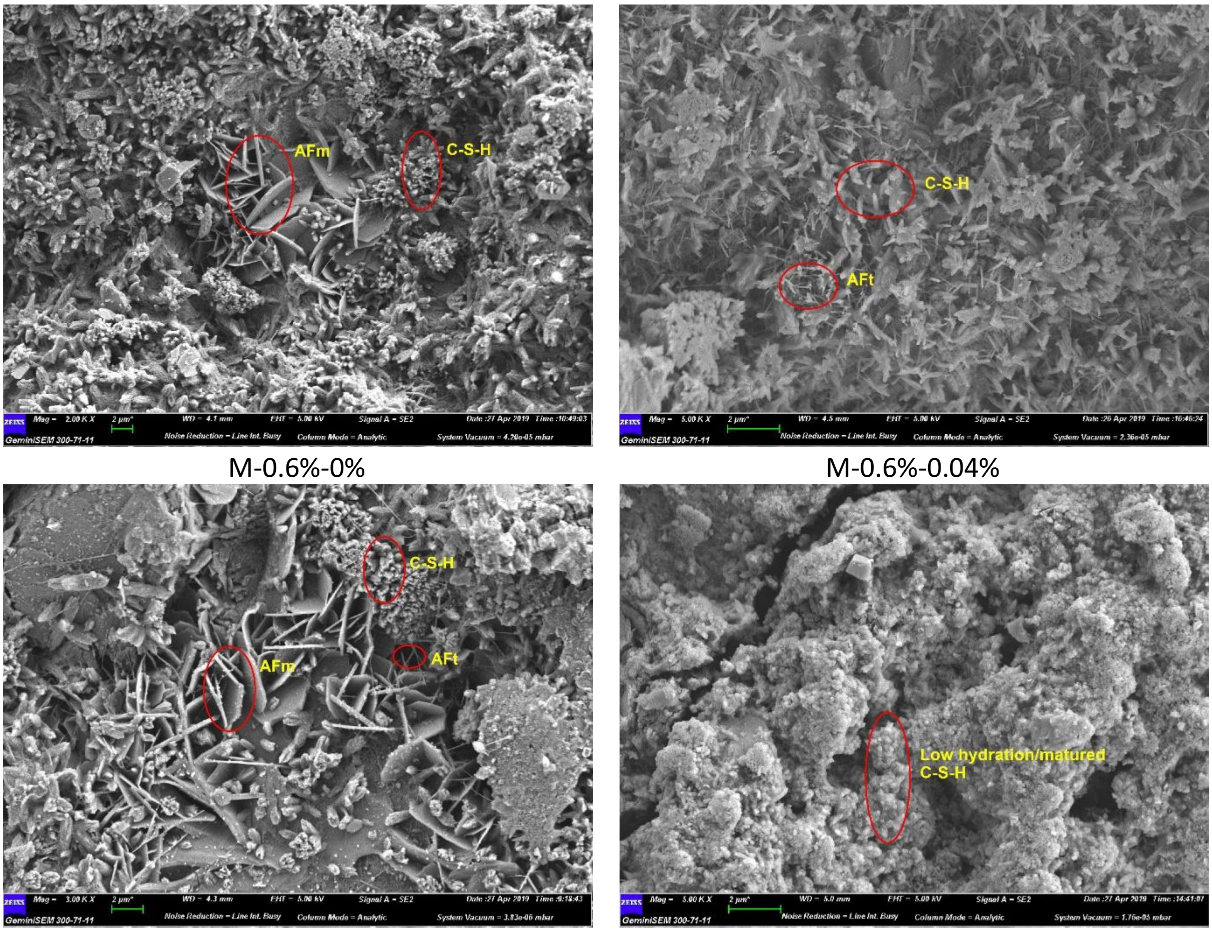

M-0.6%-0% M-0.6%-0.04%

M-0.6%-0.07% M-0-0.07%

Figure 6. SEM images presenting the hydrated phases in air-entrained mortars.

Hydrated products for air-entrained mortars detected with SEM are shown in Figure 6 for the first three samples. It was found that there are abundant C-S-H, which benefit the strength, suggesting that the mortars are hydrated sufficiently. Moreover, some AFm emerges in sample M-0.6%-0%, some AFt scattering in sample M-0.6%-0.04%, and both exist in sample M-0.6%-0.07%.

However, for sample M-0-0.07%, only low hydrated C-S-H was seen. Since the big difference of M-0-0.07% with the other samples is that it has no addition of SP, therefore, the hydration results from SEM were sufficient evidence that superplasticizers can significantly promote the hydration of air-entrained mortar. These observation results explained that the critical diameter and threshold diameter decrease with the presence of SP in the MIP section. C-S-H gel formed with the cement when hydrated, so some of the pore volume may become totally isolated due to C-S-H gel formation, thus resulting in decrease of the critical and threshold diameter.

4.3 Analysis of air-entrained concretes

4.3.1 Results from MIP

The intrusion curves for the concretes differ from those for the mortars. By comparison to the intrusion curves for mortars, the threshold of the concrete becomes less distinct and the peaks of the differential curves corresponding to the critical diameter are less sharp due to the addition of more aggregates. As explained by Winslow et al. [37], when the aggregate volume is high enough (e.g., more than 49%), the MIP cumulative curve displays two steep slopes (correspondingly, the differential curve displays bimodal distribution of pores), one due to the bulk paste and the other due to the ITZ. Correspondingly, two critical parameters, d_{c-bp} for bulk paste and d_{c-ITZ} (usually d_{c-ITZ} is 5–10 times larger than d_{c-bp}) for the ITZ are defined respectively [39]. According to the d_c^2 terms in the Katz–Thompson equation, as Equation (5) shows (assuming similar values for σ_0), the larger ITZ pores (d_{c-ITZ}) will have a more significant permeability than the small matrix pores (d_{c-bp}), which will have a significant influence on the overall permeability [44]. Usually in normal concrete, the volume fraction of aggregate is more than 60%, which allows the percolation of the ITZ, and the permeability of the concrete is governed by this ITZ percolation. Hence, d_{c-ITZ} rather than d_{c-bp}can be used to estimate the permeability together with the ITZ volume fraction.

$$\kappa_p = c \cdot \frac{\sigma}{\sigma_0} \cdot d_c^2 \tag{5}$$

where d_c is the critical pore diameter from the MIP intrusion curve, c is an analytical constant based on the pore system geometry and equal to $1/226$, σ and σ_0 are the sample and pore fluid conductivities, respectively, σ/σ_0 denotes the pore network connectivity, and κ_p is the hydraulic permeability. Since the differential curve for concrete displays a bimodal distribution of pores as elaborated above, the porosity corresponding to the first peak was defined as bulk-paste related porosity (bulk-paste porosity for short), and the second as ITZ related porosity (ITZ porosity for short) in this study (see Figure 7). Thereby, the first peak was denoted as a bulk-paste peak and the second as an ITZ peak, although in some of the literature the first peak was denoted as “capillary pores” and the second as “mesopores” [45,46].

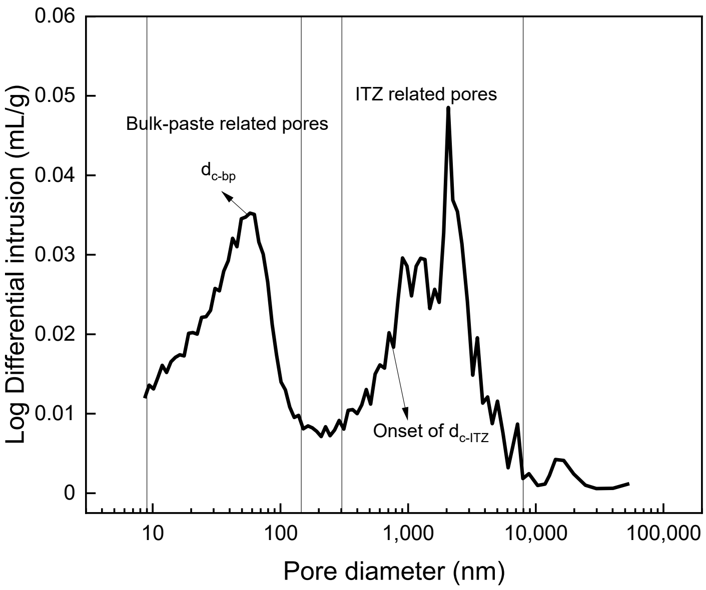

Figure 7. Definition of bulk-paste related pores and ITZ related pores for MIP analysis.

As Figure 8 displays, the cumulative plots have two slopes (as in Figure 8 (a)); bulk-paste peaks are plateaued (less sharp), while the ITZ peaks consist of a cluster of small sharp peaks that are crowded together (as in Figure 8 (b)). Therefore, it becomes difficult to trace the critical diameter d_{c-CTZ}. The onset point of the cluster of peaks was taken as d_{c-CTZ}, although this was subjective. The values of d_{c-bp}, d_{c-ITZ}, total porosity, and ITZ porosity are summarized in Table 5.

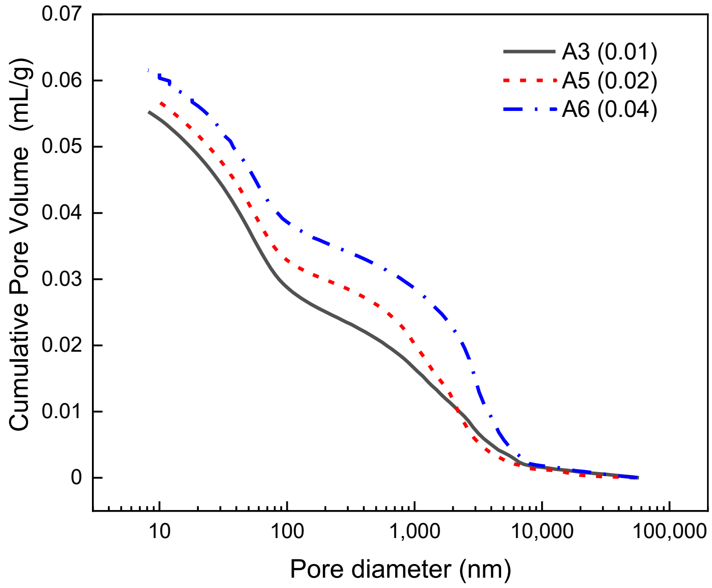

(a) Cumulative curve

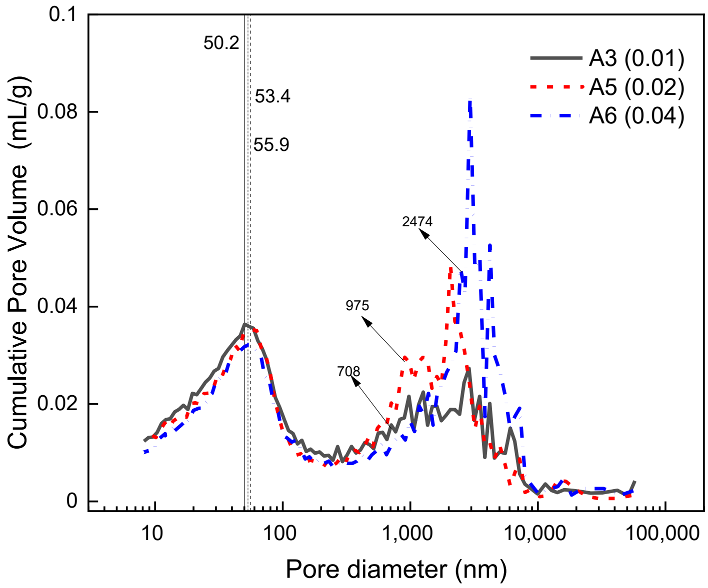

(b) Differential curve

Figure 8. Cumulative and differential curves for air-entrained concretes with different dosages of AEA.

Table 5. Parameters of concretes from MIP.

Sample no.	Total porosity (%)	ITZ porosity (%)	ITZ fraction (%)	d_{c-bp} (nm)	Onset of d_{c-ITZ} (nm)	Air content (%)
A3(0.01)	12.7	5,57	43.9	50.2	708	3.0
A5(0.02)	13.2	6.91	52.3	53.4	975	5.0
A6(0.04)	14.2	8.18	57.6	55.9	2474	6.5
B0 (0)	9.31	3.01	32.3	64.8	511	1.6
B1 (0.01)	12.0	4.81	40.1	62.3	667	3.5

Note: ITZ porosity represents the porosity related to the ITZ, which denotes the porosity of the ITZ peak covered; ITZ fraction denotes the fraction of ITZ porosity of the total porosity.

As the results have shown, the total porosity increased as the dosage of AEA increased, as was expected, but the values of $d_{c-bp}$for the bulk paste have no significant difference. However, it is worth noting that a higher dosage of AEA leads to a considerable increase (from 708 nm to 2474 nm) in the onset value of d_{c-CTZ} and the ITZ peak shifts to a coarser pore size.

Besides, the ITZ peak goes higher as the dosage of AEA increases (as displayed in Figure 8 (b)), when the aggregate fraction decreases (as shown in Table 5). The results in Table 5 show an increase in the ITZ fraction from 43.9% to 57.6% as the dosage of AEA increases. A 0.03% increase of the dosage of AEA leads to a rise of 13.7% in the ITZ fraction.

This phenomenon led to the conclusion that AEA promotes the percolation of ITZ. It was attributed to AEA that it can result in larger ITZ pores (d_{c-ITZ}) and a larger volume of ITZ porosity. This will, therefore, cause the concrete to have a significant permeability.

4.3.2 Verification

To verify the conclusion further, a comparison between another group of air-entrained concrete and blank concrete is presented in Figure 9.

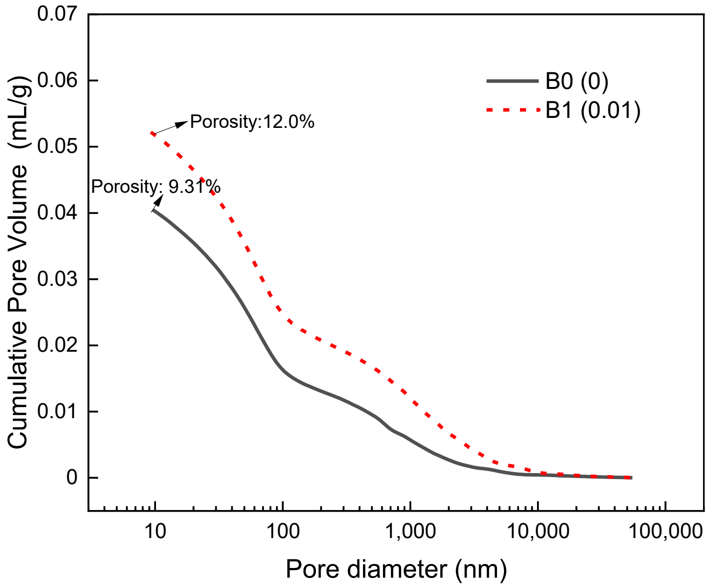

(a) Cumulative curve

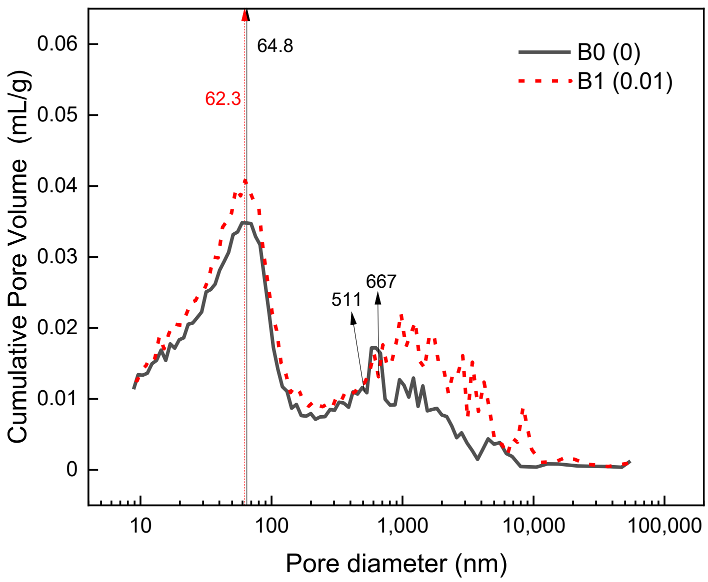

(b) Differential curve

Figure 9. Cumulative and differential curves for air-entrained concrete and blank concrete.

As expected, it is evident that the ITZ peak for the air-entrained concrete is higher and shifts to a coarser pore size (as shown in Figure 9 (b)). Also, the onset values of d_{c-CTZ} increase from 511 nm to 667 nm, and the ITZ fraction rises from 32.3% to 40.1%, as displayed in Table 5. The concrete had an approximately 8% increase in the ITZ fraction when a 0.01% dosage of AEA was used. This was evidence that the AEA promotes the percolation of ITZ. As Shane et al. have reported, the permeability of concrete is governed by the percolated ITZ [44]. The porosity of concrete is lower, but the permeability is higher than cement paste.

In addition, Matala's work in 1995 related to the pore size distribution of air-entrained concretes from MIP tests is presented in Figure 10 as a comparison of air-entrained concrete and blank concrete, and the mix composition of the related concrete is collected in Table 6.

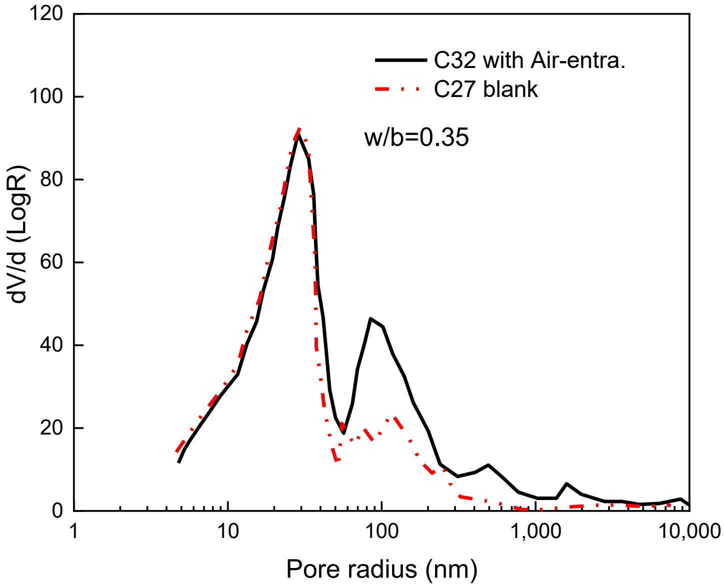

(a)

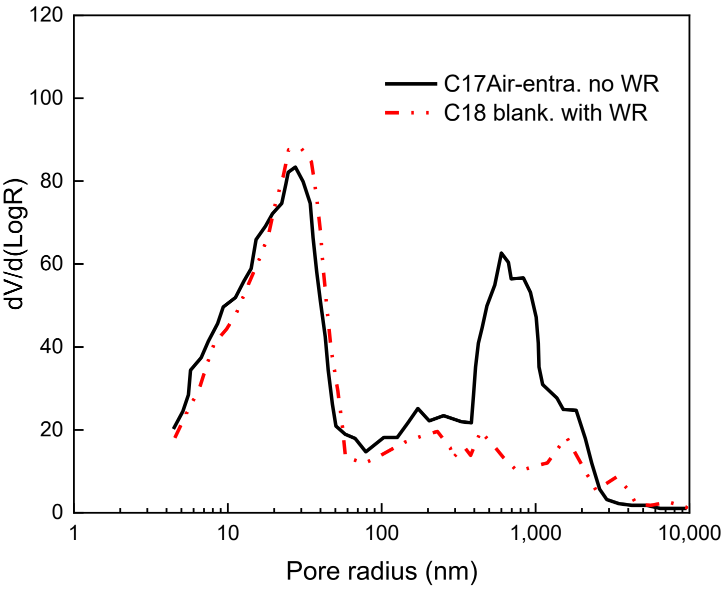

(b)

Figure 10. Pore size distribution curves of air-entrained concrete and blank concrete. Plots data are cited from Matala's PhD thesis chapter 5.4.2, Figures 17-20, pp: 66-67 [47].

Table 6. Mix composition of concretes used in Figure 10 [47].

Concrete	OPC	Water	Aggregate	Air-entr. % of binder	WR	Air (%)	W/B ratio
C32	402.3	135.8	1856.3	0.042	1.20	3.5	0.350
C27	401.2	136.4	1904.3	-	1.18	1.7	0.352
C18	405.6	179.4	1816.0	-	0.37	0.7	0.450
C17	380.9	171.4	1705.3	0.012	-	6.7	0.450

Comparing C32 and C27, the peaks for the bulk paste coincide with each other; however, it is obvious that the ITZ peak for the air-entrained concrete is higher and shifts to coarser pores coarser compared to blank concrete. This was attributed to the occurrence of air-entrained voids, along with a decrease in the aggregate fraction.

For the air-entrained concrete C17, by comparison with blank concrete C18, there is still a significantly higher ITZ peak. However, C18 has a slightly higher bulk-paste peak (it cannot coincide with that of C17), probably due to the addition of water-reducing plasticizers. It can also be observed from Figure 4 (c) and (d) that air-entrained mortar with superplasticizer has a higher peak than without it. This indicates that the SP can affect the bulk-paste peak, and it may promote the hydration of cement to some extent.

The MIP results from Matala reinforced the conclusion that AEA promotes the percolation of ITZ.

4.3.3 Correlation of the ITZ fraction and air content in air-entrained concretes

The total porosity as a function of air content as well as the dosage of AEA (dosage of air-entrainment) are presented in Figure 11 (a). The relations can be simply expressed by linear equations. For the function of air content, the value of R-square is 0.8159. The correlation between total porosity and the dosage of AEA is slightly poorer, with an R-square value of 0.7429. Similar plots using the ITZ fraction from the air content and the dosage of AEA are shown in Figure 11 (b). For the linear equation relating the ITZ fraction with the air content, the value of R-square is 0.9385, while for the correlation between the ITZ fraction and the dosage of AEA, the R-square is 0.8892.

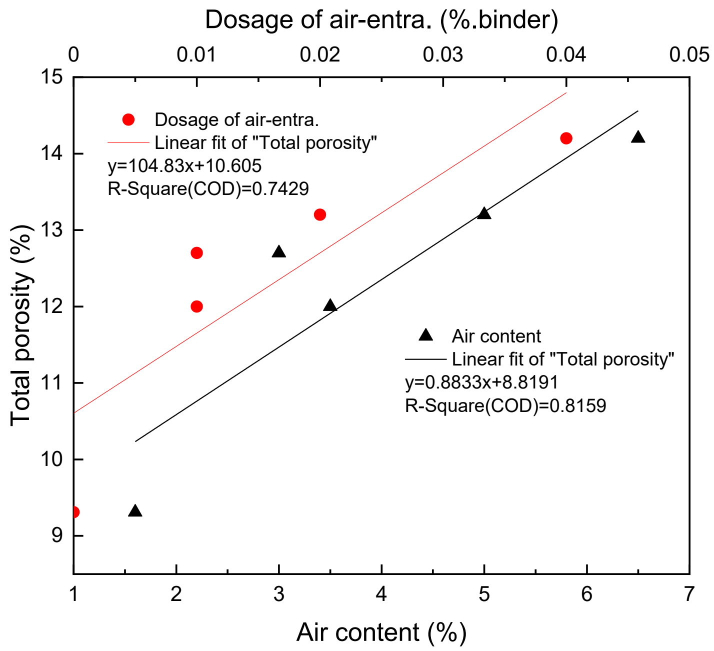

(a) Total porosity

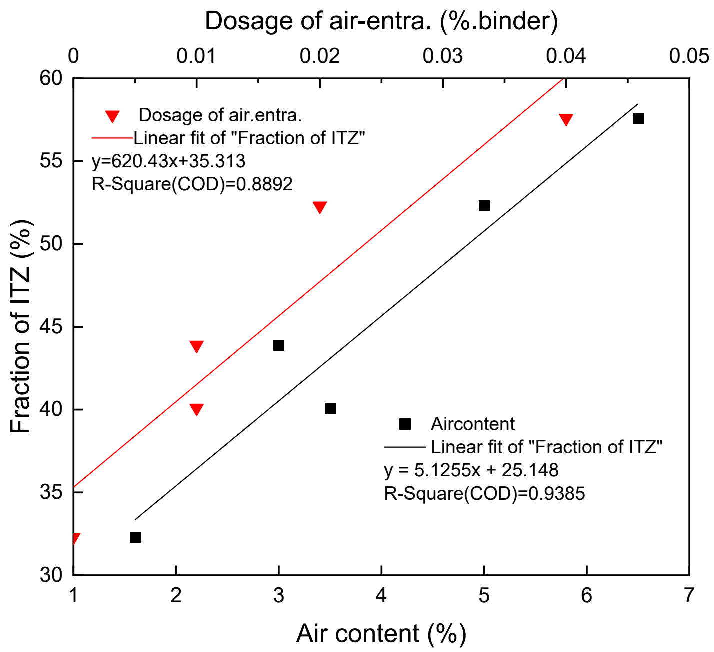

(b) Fraction of ITZ porosity

Figure 11. ITZ fraction and total porosity as a function of air content and dosage of AEA. Data are from Table 5.

The results suggest that the ITZ fraction is most correlated with the air content in air-entrained concretes. Regardless of the total porosity or ITZ fraction, both have a better correlation with the air content than with the dosage of AEA.

This high correlation between the ITZ fraction and the air content indicates that more air-entrained voids in concrete can lead to a high ITZ fraction; therefore, together with larger ITZ pores (d_{c-ITZ}), it can promote the percolation of the ITZ.

Further research is needed to cover a wider range of w/b ratios and higher additions of silica fume. Also, how the ITZ fraction and d_{c-ITZ} affect permeability, as well as the determination of the d_{c-ITZ}, are areas still needing further research.

5 Conclusions

The principal pore parameters and "ink-bottle effect" of air-entrained mortars with w/c of 0.38, having different dosages of AEA (0, 0.04, 0.07) and SP (0.0, 0.6) were investigated by MIP. Several conclusions can be drawn based on the results.

(1) The dosage of AEA does not affect the critical diameter when the SP is kept constant. But the total porosity increases as the dosage of AEA increases, and the trend of variation for total porosity is consistent with the change of air content in hardened mortar.
(2) For the air-entrained mortars, the absence of superplasticizer leads to the critical diameter and threshold diameter significantly shifting to larger pores. This may be because the C-S-H gel formed with the cement hydration; hence, some of the pore volume may become totally isolated due to C-S-H gel formation, resulting in the decrease of both the critical and threshold diameters. The SEM results evidenced that superplasticizers can significantly promote the hydration of air-entrained mortar.
(3) By comparison with other air-entrained mortars, the one with the highest content of AEA and SP has the highest values of total porosity and retention factor. This indicates that the AEA together with SP can enhance the ink-bottle effect since the tortuosity of the pores' path increased in the pore system. Besides, it was observed from SEM that this air-entrained mortar has the most uniformly distributed and reasonable size of air voids.

The influence of AEA on the pore structure of hardened concrete with higher w/c has also been studied by means of MIP. The following conclusions can be drawn.

(4) The total porosity increased as the dosage of AEA increased, as expected. However, the values of d_{c-bp} for the bulk paste show no significant difference.
(5) It is evident that the ITZ peak for air-entrained concrete goes higher and shifts to coarser pores as the entrained air increases.
(6) The ITZ fraction is most highly correlated with the air content in air-entrained concretes (with R-square of 0.9385). This high correlation between the ITZ fraction and the air content indicates that more entrained air voids in the concrete led to a high ITZ fraction; therefore, together with larger ITZ pores (d_{c-ITZ}), it can promote the ITZ percolation.

CRediT authorship contribution statement

Yanjuan Chen: Conceptualization, Methodology, Data curation, Formal analysis, Writing - review & editing. **Fahim Al-Neshawy**: Methodology, Data curation, Writing - original draft preparation. **Jouni Punkki**: Investigation, Writing - reviewing & editing.

Declaration of Competing Interest

The authors declare they have no known competing financial interests or personal relationships that could have appeared to influence the work reported in this paper.

References

[1] Bohner E, Vehmas T, Okkonen M, Kiviniemi M, Lahdenperä P, Laikari A et al. Quality Management of Concrete Construction by Digitalizing the Process Chain from Batching Plant to Building. In NDE/NDT for Highways & Bridges: SMT 2018;68-76.

[2] Chatterji S. Freezing of air-entrained cement-based materials and specific actions of air-entraining agents. Cement and Concrete Composites 2003;25:759-65.

[3] Koniorczyk M, Gawin D, Schrefler BA. Modeling evolution of frost damage in fully saturated porous materials exposed to variable hygro-thermal conditions. Computer Methods in Applied Mechanics and Engineering 2015;297:38-61.

[4] Aligizaki KK. Pore structure of cement-based materials: testing, interpretation and requirements. CRC Press, 2005.

[5] Mehta PK, Monteiro PJ, Carmona Filho A. Concreto: estrutura, propriedades e materiais. Pini, 1994.

[6] Choi P, Yeon JH, Yun K. Air-void structure, strength, and permeability of wet-mix shotcrete before and after shotcreting operation: The influences of silica fume and air-entraining agent. Cement and Concrete Composites 2016;70:69-77.

[7] Mayercsik NP, Vandamme M, Kurtis KE. Assessing the efficiency of entrained air voids for freeze-thaw durability through modeling. Cement and Concrete Research 2016;88:43-59.

[8] McCarter WJ, Forde MC, Whittington HW, Simons T. Electrical resistivity characteristics of air-entrained concrete. Proceedings of the Institution of Civil Engineers 1983;75(1):123-7.

[9] Toutanji M. Technical note The influence of air entrainment on the properties of silica fume concrete. Advances in Cement Research 1998;10:135-9.

[10] Wong HS, Pappas AM, Zimmerman RW, Buenfeld NR. Effect of entrained air voids on the microstructure and mass transport properties of concrete. Cement and Concrete Research 2011;41:1067-77.

[11] Van den Heede P, Furniere J, De Belie N. Influence of air entraining agents on deicing salt scaling resistance and transport properties of high-volume fly ash concrete. Cement and Concrete Composites 2013;37:293-303.

[12] Li W, Pour-Ghaz M, Trtik P, Wyrzykowski M, Münch B, Lura P et al. Using neutron radiography to assess water absorption in air entrained mortar. Construction and Building Materials 2016;110:98-105.

[13] Zhang P, Wittmann FH, Vogel M, Müller HS, Zhao T. Influence of freeze-thaw cycles on capillary absorption and chloride penetration into concrete. Cement and Concrete Research 2017;100:60-67.

[14] Zhang P, Li D, Qiao Y, Zhang S, Sun C, Zhao T. Effect of air entrainment on the mechanical properties, chloride migration, and microstructure of ordinary concrete and fly ash concrete. Journal of Materials in Civil Engineering 2018;30:04018265.

[15] Lutz MP, Monteiro PJ, Zimmerman RW. Inhomogeneous interfacial transition zone model for the bulk modulus of mortar. Cement and Concrete Research 1997;27:1113-1122.

[16] Gao H, Zhang X, Zhang Y. Effect of the entrained air void on strength and interfacial transition zone of air-entrained mortar. Journal of Wuhan University of Technology - Mater. Sci. Ed. 2015;30:1020-8.

[17] Ziaei-Nia A, Tadayonfar G, Eskandari-Naddaf H. Effect of air entraining admixture on concrete under temperature changes in freeze and thaw cycles. Materials Today: Proceedings 2018;5:6208-16.

[18] Edel'man LI, Sominskii DS, Kopchikova NV. Pore size distribution in cement rock. Kolloidnyi Zhurnal 1961;23:228.

[19] Olson RA, Neubauer CM, Jennings HM. Damage to the pore structure of hardened Portland cement paste by mercury intrusion. Journal of the American Ceramic Society 1997;80:2454-8.

[20] Diamond S, Bonen D. Microstructure of hardened cement paste—a new interpretation. Journal of the American Ceramic Society 1993;76:2993-9.

[21] Allen T. Particle size measurement. Springer, 2013.

[22] Van Brakel J, Modrý S, Svata M. Mercury porosimetry: state of the art. Powder Technology 1981;29:1-12.

[23] Hearn N, Hooton RD. Sample mass and dimension effects on mercury intrusion porosimetry results. Cement and Concrete Research 1992;22:970-80.

[24] Moro F, Böhni H. Ink-bottle effect in mercury intrusion porosimetry of cement-based materials. Journal of Colloid and Interface Science 2002;246:135-49.

[25] Winslow DN. Advances in experimental techniques for mercury intrusion porosimetry. In: Surface and Colloid Science. Springer, 1984, pp. 259-282.

[26] Wild S. A discussion of the paper "Mercury porosimetry-an inappropriate method for the measurement of pore size distributions in cement-based materials" by S. Diamond. Cement and Concrete Research 2001;31:1653-4.

[27] Zeng Q, Li K, Fen-Chong T, Dangla P. Pore structure characterization of cement pastes blended with high-volume fly-ash. Cement and Concrete Research 2012;42:194-204.

[28] Ye G. Experimental study and numerical simulation of the development of the microstructure and permeability of cementitious materials. 2003.

[29] Shi D, Winslow DN. Contact angle and damage during mercury intrusion into cement paste. Cement and Concrete Research 1985;15:645-54.

[30] Diamond S, Winslow DN. A mercury porosimetry study of the evolution of porosity in Portland cement. Journal of Materials 1970;5:564-85.

[31] Roy DM. Relationships between permeability, porosity, diffusion and microstructure of cement pastes, mortar, and concrete at different temperatures. MRS Online Proceedings Library Archive 1988;137.

[32] Young JF. Capillary porosity in hydrated tricalcium silicate pastes. Powder Technology 1974;9:173-9.

[33] Diamond S. Mercury porosimetry: an inappropriate method for the measurement of pore size distributions in cement-based materials. Cement and Concrete Research 2000;30:1517-25.

[34] Katz AJ, Thompson AH. Quantitative prediction of permeability in porous rock. Physical Review B 1986;34:8179.

[35] Feldman RF, Beaudoin JJ. Pretreatment of hardened hydrated cement pastes for mercury intrusion measurements. Cement and Concrete Research 1991;21:297-308.

[36] Mehta PK. Pore size distribution and permeability of hardened cement pastes. In 7th Int. Congress on Cement Chemistry. Paris;1980.

[37] Winslow DN, Cohen MD, Bentz DP, Snyder KA, Garboczi EJ. Percolation and pore structure in mortars and concrete. Cement and Concrete Research 1994;24:25-37.

[38] Liu Z, Winslow D. Sub-distributions of pore size: a new approach to correlate pore structure with permeability. Cement and Concrete Research 1995;25:769-78.

[39] Ma H. Mercury intrusion porosimetry in concrete technology: tips in measurement, pore structure parameter acquisition and application. Journal of Porous Materials 2014;21:207-15.

[40] Winslow D. Some experimental possibilities with mercury intrusion porosimetry. MRS Online Proceedings Library Archive 1988;137.

[41] Feldman RF. Pore structure damage in blended cements caused by mercury intrusion. Journal of the American Ceramic Society 1984;67:30-3.

[42] Hill RD. A study of pore size distribution of fired clay bodies. 11. An improved method of interpreting mercury penetration data, Trans. Brit. Ceram. Soc. 1960;59:198-212.

[43] Ritter HL, Erich LC. Pore size distribution in porous materials. Analytical Chemistry 1948;20:665-70.

[44] Shane JD, Mason TO, Jennings HM, Garboczi EJ, Bentz DP. Effect of the interfacial transition zone on the conductivity of Portland cement mortars. Journal of the American Ceramic Society 2000;83:1137-44.

[45] Cwirzen A, Penttala V. Aggregate–cement paste transition zone properties affecting the salt–frost damage of high-performance concretes. Cement and Concrete Research 2005;35:671-9.

[46] Penttala VE. Effects of microporosity on the compression strength and freezing durability of high-strength concretes. Magazine of Concrete Research 1989;41:171-81.

[47] Matala S. Effects of carbonation on the pore structure of granulated blast furnace slag concrete. Helsinki University of Technology, 1995.